Motion Estimation under Location Uncertainty for Turbulent Fluid Flow

Shengze Cai, Etienne Mémin, Pierre Dérian, Chao Xu

Experiments in Fluids manuscript No.
(will be inserted by the editor)

Motion Estimation under Location Uncertainty for Turbulent Fluid Flows

Shengze Cai · Etienne Mémin · Pierre Dérian · Chao Xu

Received: date / Accepted: date

Abstract In this paper, we propose a novel optical flow formulation for estimating two-dimensional velocity fields from an image sequence depicting the evolution of a passive scalar transported by a fluid flow. This motion estimator relies on a stochastic representation of the flow allowing to incorporate naturally a notion of uncertainty in the flow measurement. In this context, the Eulerian fluid flow velocity field is decomposed into two components: a large-scale motion field and a small-scale uncertainty component. We define the small-scale component as a random field. Subsequently, the data term of the optical flow formulation is based on a stochastic transport equation, derived from the formalism under location uncertainty proposed in Mémin (2014) and Resseguier et al. (2017a). In addition, a specific regularization term built from the assumption of constant kinetic energy involves the very same diffusion tensor as the one appearing in the data transport term. Opposite to the classical motion estimators, this enables us to devise an optical flow method dedicated to fluid flows in which the regularization parameter has now a clear physical interpretation and can be easily estimated. Experimental evaluations are presented on both synthetic and real world image sequences. Results and comparisons indicate very good performance of the proposed formulation for turbulent flow motion estimation.

This work was supported in part by the National Natural Science Foundation of China under Grant 61473253, and in part by the Foundation for Innovative Research Groups of the National Natural Science Foundation of China under Grant 61621002.

S. Cai · C. Xu
State Key Laboratory of Industrial Control Technology and the Institute of Cyber-Systems & Control, Zhejiang University, Hangzhou, 310027 Zhejiang, China.
E-mail: szcai, cxu@zju.edu.cn
Corresponding author: Chao Xu

E. Mémin · P. Dérian
National Institute for Research in Computer Science and Control (INRIA), Campus Universitaire de Beaulieu, 35042 Rennes, France.
E-mail: etienne.memin, pierre.derian@inria.fr

1 Introduction

With the development of technology, motion estimation techniques are becoming increasingly important in the study of fluid dynamics. Extracting the velocity fields from image sequences, whether provided by experimental facilities or meteorological and oceanographical satellites, allows the researchers to get a deeper insight into the complex and unsteady fluid flow velocity fields.

Among the flow visualization techniques, particle image velocimetry (PIV) is the most commonly used to estimate velocity fields from images. Small particles are seeded into the flow. A laser sheet illuminates the flow domain, then successive images with fluorescent particles are recorded by a camera. Eventually, by searching the maximum of the cross-correlation between two interrogation windows of an image pair, the displacement vectors of the investigated flow are obtained. Such a correlation-based PIV technique is well-established and widely-used. A thorough description on advanced PIV principles can be found in the text book (Raffel et al., 2007).

Despite its simplicity and efficiency, there are several limitations of cross-correlation (CC) PIV. For instance, the spatial resolution of the resulting velocity field mainly depends on the size of the interrogation windows. Large window size leads to motion fields with low resolution and with no small-scale structures. Furthermore, the correlation-based techniques are in general not suitable for scalar diffusion pictures such as laser induced fluorescence (LIF) images, which exhibit large areas with low photometric gradients, where the correlation peak is hard to estimate correctly by CC techniques.

In recent years, optical flow computation has been considered as a promising alternative to supplement traditional cross-correlation techniques in such a context. First proposed by Horn and Schunck (1981), optical flow has been intensively studied in the computer vision community, and a huge number of variations and improvements have been presented in the literature, such as Black and Anandan (1996), Mémin and Pérez (1998), Brox et al. (2004), Bruhn et al. (2005), Sun et al. (2010). All these methods rely on the fundamental assumption of a brightness conservation along a point trajectory:

$$\frac{\mathrm{d}f}{\mathrm{d}t} = \frac{\partial f}{\partial t} + \nabla f \cdot \boldsymbol{\omega} = 0. \tag{1}$$

In this transport equation, referred to as the optical flow constraint (OFC) equation, ∇ denotes the gradient operator in two dimensional directions, f and $\boldsymbol{\omega}$ the intensity of the image and the motion field, respectively. For dense optical flow approaches, the OFC equation is associated with a spatial coherency assumption (Horn and Schunck, 1981), in order to cope with the underconstrained vectorial estimation problem associated with this scalar equation – so called the aperture problem in the computer vision literature. A weighting coefficient balances these two terms in the optic-flow energy functional.

Compared to the cross-correlation PIV approaches, which provide sparse motion measurements, optical flow methods enable to estimate dense velocity fields. These latter techniques thus potentially lead to motion fields with finer details. In addition, the OFC equation (1) can be considered as an evolution law describing the transportation of a fluidic scalar by a motion field. This property allows to combine various physical constraints more easily, and also to directly deal with images of a transported scalar instead of particle images. Comparisons between the optical flow and the cross-correlation methods in extracting velocity fields from particle images have been presented in Liu et al. (2015). Despite their differences, PIV and optical flow estimators both rely on a strong smoothing constraint – either implicitly given through a locally constant velocity in PIV or explicitly formulated through the regularization smoothing term in optic-flow methods. This constraint even formulated in a fluid flow context (Corpetti et al., 2006) is difficult to interpret physically. Even worse, the solution highly depends on the weighting coefficients chosen (corresponding to the interrogation window size in PIV).

The original Horn and Schunck (HS) formulation has been extended in various ways in order to cope with fluid motion estimation. One of the earliest attempts can be traced back to Quénot et al. (1998), where an optical flow technique with dynamic programming constraints was applied to particle image velocimetry. Ruhnau et al. (2005) proposed a multi-resolution variational optical flow approach for particle images as well. Corpetti et al. (2002, 2006) presented a fluid-flow dedicated formulation based on the integrated continuity equation (ICE) and a second-order *div-curl* regularizer, that can preserve better the divergence and the vorticity of the flow. Liu and Shen (2008) discussed exhaustively the relation between optical flow and fluid flow, and suggested to use the projected motion equation. Heitz et al. (2008) applied the generalized transport equation, and combined cross-correlation with optical flow approach to make the estimation more robust. Among the recently-developed techniques, optical flow is also formulated in the forms of orthogonal decomposition (Yuan et al., 2007; Stapf and Garbe, 2014), wavelet expansion with a higher-order regularization term (Dérian et al., 2013; Kadri-Harouna et al., 2013), optimal control scheme (Papadakis and Mémin, 2008) or Bayesian stochastic filtering approach (Cuzol and Mémin, 2009; Beyou et al., 2013; Papadakis et al., 2010). A review which provides more descriptions and comparisons of different estimation techniques is presented by Heitz et al. (2010).

Despite a great research effort, turbulence modeling and measurement is still a very challenging issue in experimental fluid mechanics. Realistic turbulent flows contain small-scale structures that are significant for energy and mass transport. However, these sub-grid scales are rubbed out through the regularization term. The small-scale effects are in addition not taken into account in the OFC equation. This is all the more prejudicial to an accurate estimation when the image grid or the frame rate corresponds to a large-scale resolution of the fluid flow – such as in the case of oceanic or atmospheric satellite images. Therefore, in order to estimate the motion of turbulent flows from images, turbulence models should be specifically introduced. So far, there have been only few works that addressed this challenge. Cassisa et al. (2011) replaced the optical flow constraint with a sub-grid transport equation by introducing an eddy-diffusivity model. However, the diffusion coefficient of the transport equation is fixed and selected empirically. Instead, Chen et al. (2015) suggested to apply a structural sub-grid model with an eddy viscosity for computing the small-scale diffusion term. The work of Chen et al. (2015) improves the estimation results. These works indicate that the combination of turbulence models and the variational optical flow schemes is a very promising direction. Let us however outline that these approaches still highly depend on a regularization parameter whose value is difficult to fix and which has no direct physical interpretation. Note also that a second parameter weighting the considered turbulence model is added in the data model. Though this parameter has generally a precise form derived with an isotropic turbulence assumption (Lilly, 1966), the precise value of this parameter is difficult to fix in practice.

In this paper, we aim at proposing a novel formulation for turbulent fluid motion estimation with a different strategy. The main ideas and contributions of this work consist in

reformulating the optical flow estimation problem through the introduction of uncertainties and the modeling under location uncertainty. As derived by Mémin (2014), the Eulerian velocity of a flow is decomposed into a large-scale component and a rough small-scale turbulent component. The latter one, specified as a random field and referred to as location uncertainty, gives rise to a modified transport equation (Resseguier et al., 2017a) obtained from a stochastic expression of the Reynolds transport theorem (Crisan et al., 2017; Mémin, 2014). A similar expression could be as well obtained from a variational principle (Holm, 2015). The resulting stochastic optical flow constraint equation includes directly in its representation the effects of the small scales. Another constraint on the kinetic energy enables us to interpret the regularization term as a physical constraint. As we will demonstrate in this paper, all the parameters involved in this optical flow model can be optimally set. The resulting estimator can be hence finally considered as a parameter-free approach. There is no need to resort the inescapable and cumbersome tuning of the smoothing-parameter associated to classical motion estimation cost functions.

The rest of this paper is organized as follows. In Section 2, the optical flow formulation under location uncertainty is derived in detail. Then the implementation settings and minimization scheme are described in Section 3. Experimental evaluations on synthetic images and real data are demonstrated in Section 4 and Section 5, respectively. Comparisons with other fluid motion estimation techniques are also given in these sections. Eventually, conclusion is discussed in Section 6.

2 Methodology Description

2.1 Stochastic transport

Let $\mathbf{x}_t = (x,y)^T$ ($\mathbf{x}_t \in \mathbb{R}^2$) denote the position of a particle in the two-dimensional (2D) domain Ω at time step t. To derive the transport under location uncertainty, we follow the basic assumption that the Eulerian velocity field of turbulent flow consists of a smooth velocity component $\omega(\mathbf{x},t) = (u,v)^T$ and a small-scale random velocity component termed uncertainty. Accordingly, the Lagrangian stochastic displacement regarding the trajectory $\mathbf{x}_t$ reads:

$$\mathrm{d}\mathbf{x}_t = \omega(\mathbf{x}_t,t)\mathrm{d}t + \sigma(\mathbf{x}_t,t)\mathrm{d}\mathbf{B}_t, \tag{2}$$

or in an integral form

$$\mathbf{x}_t = \mathbf{x}_{t_0} + \int_{t_0}^{t} \left[\omega(\mathbf{x}_s,s)\mathrm{d}s + \sigma(\mathbf{x}_s,s)\mathrm{d}\mathbf{B}_s\right]. \tag{3}$$

Note that (2) is a stochastic differential equation and (3) is one of the integral representations among many, i.e., the Ito integral. In fluid dynamics, the term $\sigma\mathrm{d}\mathbf{B}_t$ denotes the unresolved small-scale velocity fluctuation of turbulent flow. This expression involves a multidimensional random function, $\mathbf{B}_t$, that can be interpreted as a white noise process in space and a Brownian process in time. The spatial correlations of the velocity uncertainty are specified through a diffusion operator $\sigma(\mathbf{x},t)$ defined through the matrix kernel $\breve{\sigma}(\cdot,\cdot,t)$ for any vectorial function $\boldsymbol{f}$ (n-dimensional) as:

$$\sigma(\mathbf{x},t)\boldsymbol{f} \triangleq \int_{\Omega} \breve{\sigma}(\mathbf{x},\mathbf{z},t)\boldsymbol{f}(\mathbf{z},t)\mathrm{d}\mathbf{z}. \tag{4}$$

Therefore, it can be seen that this operator is a matrix mapping from $\mathbb{R}^n$ into $\mathbb{R}^2$ at point $\mathbf{x}$. In a motion estimation context, the flow velocity field is assumed constant between two successive image frames. Although this leads to a time-averaged estimation, the assumption also stands for unsteady flows as long as the time interval between two samples $\mathrm{d}t$ is small. Then without loss of generality we can safely ignore the time variable of $\omega(\mathbf{x},t)$ and $\sigma(\mathbf{x},t)$:

$$\mathrm{d}\mathbf{x} = \omega(\mathbf{x})\mathrm{d}t + \sigma(\mathbf{x})\mathrm{d}\mathbf{B}_t, \tag{5}$$

where $\mathrm{d}\mathbf{x} = \mathbf{x}_t - \mathbf{x}_{t-1}$ represents the displacements of particles between two successive images. The uncertainty component, $\sigma(\mathbf{x})\mathrm{d}\mathbf{B}_t$, representing the small-scale velocity will be assumed to be incompressible (i.e., $\nabla \cdot \sigma(\mathbf{x})\mathrm{d}\mathbf{B}_t = 0$) in this paper. This component is a Gaussian random function correlated in space and uncorrelated in time. The covariance tensor of the uncertainty component $\sigma\mathrm{d}\mathbf{B}_t$ (namely correlation tensor at different locations within the physical domain - $\mathbf{x}$ and $\mathbf{x}'$) reads:

$$\begin{aligned} Q = Cov(\mathbf{x},\mathbf{x}') &\triangleq \mathbb{E}\left[(\sigma(\mathbf{x})\mathrm{d}\mathbf{B}_t)(\sigma(\mathbf{x}')\mathrm{d}\mathbf{B}_t)^T\right] \\ &= \int_{\Omega} \breve{\sigma}(\mathbf{x},\mathbf{z})\breve{\sigma}(\mathbf{z},\mathbf{x}')\mathrm{d}\mathbf{z}\,\mathrm{d}t \\ &= \sigma(\mathbf{x})\sigma^T(\mathbf{x}')\,\mathrm{d}t, \end{aligned} \tag{6}$$

where $\mathbb{E}\left[(\mathrm{d}\mathbf{B}_t)(\mathrm{d}\mathbf{B}_t)^T\right] = \mathrm{d}t$. The diagonal of the covariance tensor, $\boldsymbol{a}$, is referred to as the variance tensor:

$$\boldsymbol{a}(\mathbf{x}) \triangleq \sigma(\mathbf{x})\sigma^T(\mathbf{x}) = \int_{\Omega} \breve{\sigma}(\mathbf{x},\mathbf{z})\breve{\sigma}(\mathbf{z},\mathbf{x})\mathrm{d}\mathbf{z} = \frac{Cov(\mathbf{x},\mathbf{x})}{\mathrm{d}t}. \tag{7}$$

Note that $\boldsymbol{a}$ is actually defined by the single-point covariance of the small-scale displacement. It is a 2×2 symmetric positive definite matrix for each spatial point $\mathbf{x}$ in the physical domain Ω. The trace of these matrices represents (up to a decorrelation time) the turbulent kinetic energy. Given the uncertainty formalism, we now consider that a conserved scalar quantity f is transported by a motion field under location uncertainty introduced above. Then the conservation law reads:

$$f(\mathbf{x}_t + \mathrm{d}\mathbf{x}_t, t+\mathrm{d}t) = f(\mathbf{x}_t,t). \tag{8}$$

The conservation law is restricted to a 2D domain in this paper, since we assume that the out-of-plane velocity component and diffusion effect are comparatively small. As f is

assumed to be conserved only up to an unresolved component and is also a random function, its material derivative $D_t f \triangleq \mathrm{d}(f(\mathbf{x},t))$, which involves the composition of two stochastic processes, can be derived from the stochastic calculus (Ito-Wentzell formula). Before giving the expression of the material transport equation $D_t f$, we first introduce the stochastic transport operator defined as follows:

$$\mathbb{D}_t f = \mathrm{d}_t f + \nabla f \cdot (\omega^* \mathrm{d}t + \sigma \mathrm{d}\mathbf{B}_t) - \frac{1}{2}\nabla \cdot (\boldsymbol{a}\nabla f)\mathrm{d}t, \tag{9}$$

where $\mathrm{d}_t f$ stands for the time increment of the (non differentiable) quantity f: $\mathrm{d}_t f = f(x,t+\mathrm{d}t) - f(x,t)$ and ω^* is the modified large-scale velocity that takes into account the inhomogeneity of the small-scale noise. It is given by

$$\omega^* = \omega - \frac{1}{2}(\nabla \cdot \boldsymbol{a})^T. \tag{10}$$

This velocity corresponds to a correction of the large-scale velocity by a small-scale velocity component induced by the small scales inhomogeneity. The induced statistical velocity $(\nabla \cdot \boldsymbol{a})$ is a drift going from the variance tensor maxima to the variance tensor minima. It is related to a phenomenon called *turbophoresis* in inhomogeneous turbulence. For homogeneous turbulence model this term does not come into play (as $\boldsymbol{a}$ is constant).

The transport operator $\mathbb{D}_t f$ is directly related to the material derivative $D_t f$. Explicit link between them is presented in Resseguier et al. (2017a), here we give the conclusion. In the general case the former has always an explicit expression whereas the latter has a clear physical meaning but no explicit expression. However, for an incompressible random term ($\nabla \cdot \sigma \mathrm{d}\mathbf{B}_t = 0$) and when the quantity is transported or conserved within a material volume (such as the mass), both operators coincide (Resseguier et al., 2017a):

$$\begin{aligned} D_t f &= \mathbb{D}_t f \\ &= \mathrm{d}_t f + \nabla f \cdot (\omega^* \mathrm{d}t + \sigma \mathrm{d}\mathbf{B}_t) - \frac{1}{2}\nabla \cdot (\boldsymbol{a}\nabla f)\mathrm{d}t, \\ &= \mathrm{d}_t f + \left[\nabla f \cdot \omega^* - \frac{1}{2}\nabla \cdot (\boldsymbol{a}\nabla f)\right]\mathrm{d}t + \nabla f \cdot \sigma \mathrm{d}\mathbf{B}_t. \end{aligned} \tag{11}$$

This formulation, originally derived from the conservation law (8), has been recently used successfully to define large scale models for large eddies simulation (Kadri-Harouna and Mémin, 2017), to provide reduced order model with data driven small-scale dissipation terms (Resseguier et al., 2017d) and to derive large-scale stochastic dynamics for geophysical fluids (Resseguier et al., 2017a,b,c). Compared to the deterministic material derivative, several additional terms related to the uncertainty random field are now involved. As mentioned previously, the scalar is advected by a modified drift ω^*. A transport by the small scale component is also visible in the last right-hand side term of (11). The uncertainty term has also a mixing effect on the large-scale motion through a diffusion term along the proper directions of the variance tensor (third term of the right-hand side of (11)). In the next section this expression of the material derivative enables us to derive an optical flow constraint under location uncertainty.

2.2 Data term based on stochastic model

From the previous stochastic transport equation, a novel observation term for optical flow estimation can be proposed. Hereafter, the conserved quantity f is assumed to be proportional to the image intensity. Since the Brownian random terms have zero mean, one can take the expectation of (11) to derive the mean scalar advection, namely

$$\begin{aligned} \mathbb{E}(\mathbb{D}_t f) &= \mathbb{E}\left[\mathrm{d}_t f + \left(\nabla f \cdot \omega^* - \frac{1}{2}\nabla \cdot (\boldsymbol{a}\nabla f)\right)\mathrm{d}t\right] \\ &= \left[\partial_t \mathbb{E}(f) + \nabla \mathbb{E}(f) \cdot \omega^* - \frac{1}{2}\nabla \cdot (\boldsymbol{a}\nabla \mathbb{E}(f))\right]\mathrm{d}t \end{aligned} \tag{12}$$

The data term of the motion estimation cost function can be set as the variance of the luminance variation:

$$\begin{aligned} e_{data} =& \mathbb{E}[(\mathbb{D}_t f - \mathbb{E}(\mathbb{D}_t f))^2] \\ \approx& \int_\Omega \left[\mathrm{d}_t f + \left(\nabla f \cdot \omega^* - \frac{1}{2}\nabla \cdot (\boldsymbol{a}\nabla f)\right)\mathrm{d}t\right]^2 \mathrm{d}\mathbf{x} \\ &- \int_\Omega \beta^2 \left[(\nabla f)^T \boldsymbol{a}(\nabla f)\mathrm{d}t\right]\mathrm{d}\mathbf{x}. \end{aligned} \tag{13}$$

The derivations in (13) are thoroughly given in Appendix A, where an additional coefficient β has to be fixed or estimated. An estimator of this coefficient is provided in Appendix A. As all the quantities involved are assumed to be constant in time between two consecutive images, $\mathrm{d}t$ is replaced by the time interval between the two frames and non-dimensionalized to 1. If the investigated flow is fully resolved or contains no location uncertainty (i.e., the variance factor of the uncertainty component $\boldsymbol{a} = \mathbf{0}$), the simplified version of (13) boils down exactly to the classical optical flow constraint equation. The data model is the sum of two quadratic terms. The first one has the form of a modified OFC equation. This new brightness consistancy model includes a modified drift and a diffusion of the image brightness. The modified drift and the diffusion represents the unresolved scales action on the velocity field. They are driven respectively by the divergence and the proper directions of the variance tensor. As for the second term, it can be observed that it corresponds to a weighting of the scalar energy dissipation. It can be thus seen as the measure of the mean scalar energy evolution on the time interval between two consecutive images.

2.3 Regularization term dedicated to stochastic transport

Generally, the regularization term in motion estimation cost functionals is set from a regularity condition on the solution. In general, such assumption is difficult to relate to kinematical or dynamical properties of the flow. In this section, we derive a spatial regularizer ensuing from an energy conservation assumption, which will be combined with (13) to form the final objective functional. Based on the stochastic transport presented in Section 2.1, a stochastic representation of the Navier-Stokes equations has been derived in Mémin (2014). By neglecting the external forces, the dynamics of the stochastic flow (namely momentum equation under location uncertainty) has the following expression:

$$\frac{\partial \omega_i}{\partial t} + (\omega^* \cdot \nabla)\,\omega_i - \frac{1}{2}\nabla \cdot (\boldsymbol{a}\nabla\omega_i) = 0, \tag{14}$$

where ω^* and $\boldsymbol{a}$ are defined in the same way as (11), and i stands for the component of x-direction or y-direction, i.e., $\omega_i = u$ or v. An inner product with the velocity of equation (14) followed by integrations by parts provides the kinetic energy evolution:

$$\frac{\partial}{\partial t}E_{kin} = \frac{1}{2}\frac{\partial}{\partial t}\parallel \omega \parallel_2^2 = -\frac{1}{2}\int_\Omega \sum_i \left[(\nabla\omega_i)^T \boldsymbol{a}(\nabla\omega_i)\right] \mathrm{d}\mathbf{x}. \tag{15}$$

In order to obtain a transformation from one image to the subsequent one that tends to conserve the kinetic energy, we can expect the norm appearing in the right-hand-side of (15) to be as small as possible, i.e.,

$$e_{reg} = \frac{1}{2}\int_\Omega \left[(\nabla u)^T \boldsymbol{a}(\nabla u) + (\nabla v)^T \boldsymbol{a}(\nabla v)\right] \mathrm{d}\mathbf{x}. \tag{16}$$

We may remark that the regularizer (16) is the same as the usual gradient penalizer when the small-scale diffusion tensor, $\boldsymbol{a}$, is the identity. Therefore, the classical gradient smoothing penalization can be interpreted as derived from a homogeneous divergence-free uncertainty random field (Mémin, 2014). This basic model yields a smoothing with no preferential direction. With an inhomogeneous variance tensor, this regularization term can be considerably enriched to drive the diffusion toward meaningful directions.

Remark 1 It is necessary to discuss here the unit of the covariance factor $\boldsymbol{a}$. According to the principle that different terms in a physical equation should have the same unit, we now examine the units of the different terms in the momentum transport equation (14). By letting $\lceil g \rfloor$ denote the unit of function g, we have:

$$\lceil \frac{\partial \omega}{\partial t} \rfloor = \frac{L}{T^2},$$

where L and T denote the basic units of length and time, respectively. That means the unit of the third term in (14) should satisfy:

$$\lceil \nabla \cdot (\boldsymbol{a}\nabla\omega) \rfloor = \lceil \boldsymbol{a} \rfloor \cdot \lceil \Delta\omega \rfloor = \lceil \boldsymbol{a} \rfloor \cdot \frac{1}{TL} = \frac{L}{T^2}.$$

Hence, we obtain

$$\lceil \boldsymbol{a} \rfloor = \frac{L^2}{T}, \tag{17}$$

which could have been obtained directly from the variance tensor definition. Furthermore, by substituting (17) into the data term (13) and the regularization term (16) discussed above, we have:

$$\lceil e_{data} \rfloor = \frac{I^2}{T^2}, \quad \lceil e_{reg} \rfloor = \frac{L^2}{T^3}, \tag{18}$$

where I denotes the basic unit of the intensity, and in practice, the unit of time is non-dimensionalized with the time difference between two consecutive images and therefore set to 1. To balance these two terms, a weighting coefficient λ with unit $\frac{I^2 T}{L^2}$ must be introduced.

Gathering the data term and the regularization term, the final energy function we will consider in this work reads:

$$\begin{aligned} J =& e_{data} + \lambda e_{reg} \\ =& \int_\Omega \left(\mathrm{d}_t f + \nabla f \cdot \omega^* - \frac{1}{2}\nabla \cdot (\boldsymbol{a}\nabla f)\right)^2 \mathrm{d}\mathbf{x} \\ & - \int_\Omega \beta^2 (\nabla f)^T \boldsymbol{a}(\nabla f) \mathrm{d}\mathbf{x} \\ & + \lambda \int_\Omega \frac{1}{2}\left[(\nabla u)^T \boldsymbol{a}(\nabla u) + (\nabla v)^T \boldsymbol{a}(\nabla v)\right] \mathrm{d}\mathbf{x}, \end{aligned} \tag{19}$$

where λ is a positive weight coefficient. In traditional optical flow methods the weighting parameter balancing the data term and the regularizer is a very sensible parameter that is difficult to tune. In general, the accuracy of the results highly depends on the value of λ. In practice, this parameter is fixed manually on a successive trial basis. The tuning procedure is all the more difficult since λ is not related to any physical quantity such as the motion amplitude, or a characteristic value of the intensity function or of its gradients. In this paper, by dimensional analysis of the objective functional (discussed in Remark 1), we find that λ should have the unit of $\frac{I^2}{L^2}$ (the unit of time is set to 1). That means λ can be related to the gradient of image intensity. Therefore, from this point of view, one possible choice consists to formulate λ as:

$$\lambda = \frac{1}{\Omega}\int_\Omega \frac{(\mathrm{d}_t f)^2}{(L_{\max})^2} \mathrm{d}\mathbf{x}, \tag{20}$$

where $L_{\max}$ represents the length scale in the images, which is given by the maximum magnitude of the apparent displacements.

2.4 Uncertainty model

As previously mentioned, there is possibly a lot of degrees of freedom to define the tensor $\boldsymbol{a}$, which appears both in the data term and in the regularization term. This opens possibilities to estimate eventually the parameters associated to a given variance model. In this study, in order to demonstrate the potential of this formalization we will consider a simple isotropic divergence free model. This condition leads to a constant uncertainty for the whole domain between two successive samples, i.e.,

$$\boldsymbol{a}(\mathbf{x}) = \alpha \mathbb{I}_2 = \text{const.},$$

where $\mathbb{I}_2$ is the 2×2 identity matrix, hence $\nabla\cdot\boldsymbol{a}(\mathbf{x})=0$ and then $\omega^* = \omega$ due to (10). Therefore, in this case the stochastic transport equation (11) can be simplified as follow:

$$D_t f = \mathbb{D}_t f = \mathrm{d}_t f + \left(\nabla f\cdot\omega - \frac{1}{2}\alpha\Delta f\right)\mathrm{d}t + \nabla f\cdot\sigma\mathrm{d}\mathbf{B}_t = 0, \tag{21}$$

where Δ is the Laplacian operator. Likewise, the energy functional for optical flow computation, simplified from (19), can be obtained:

$$\begin{aligned} J = &\int_\Omega \left[\left(\mathrm{d}_t f + \nabla f\cdot\omega - \frac{1}{2}\alpha\Delta f\right)^2 - \beta^2\alpha|\nabla f|^2\right]\mathrm{d}\mathbf{x} \\ &+ \int_\Omega \frac{1}{2}\lambda\alpha \mid \nabla\omega\mid^2 \mathrm{d}\mathbf{x}, \end{aligned} \tag{22}$$

where $|\cdot|$ denotes the Euclidean norm, and $\mid\nabla\omega\mid^2 = \mid\nabla u\mid^2 + \mid\nabla v\mid^2$ (e.g., $\mid\nabla u\mid^2 = (\partial_x u)^2 + (\partial_y u)^2$). The resulting energy functional resembles to a simple modification of the Horn & Schunck functional. However, in the new formulation, the penalization constant of the smoothing term is now interpreted as the variance of the small-scale unresolved motion (up to a dimensional constant that can be fixed easily - see the previous section). This variance parameter now also appears as the weighting factor of two additional terms in the data adequacy terms. As explained in the next section, this property will allow us to estimate the variance parameter efficiently.

3 Minimization and Implementation

In this section we compute the minimum solution in details of the cost functional with respect to the two unknowns: ω and α. The optimization algorithm is performed through an alternated minimization of the two variables.

3.1 Minimization with respect to the motion field

Let $\mathrm{d}_t f \triangleq f_t$, $\nabla f = (\partial_x f, \partial_y f) \triangleq (f_x, f_y)$. According to the calculus of variation (Euler-Lagrange equation), we have

$$\begin{cases} \dfrac{\partial J}{\partial u} - \dfrac{\partial}{\partial x}\dfrac{\partial J}{\partial u_x} - \dfrac{\partial}{\partial y}\dfrac{\partial J}{\partial u_y} = 0, \\ \dfrac{\partial J}{\partial v} - \dfrac{\partial}{\partial x}\dfrac{\partial J}{\partial v_x} - \dfrac{\partial}{\partial y}\dfrac{\partial J}{\partial v_y} = 0. \end{cases} \tag{23}$$

Then, by substituting (22) into (23), we can readily obtain

$$\begin{cases} 2\left(f_x u + f_y v + f_t - \dfrac{1}{2}\alpha\Delta f\right) f_x - 2\cdot\dfrac{1}{2}\lambda\alpha\Delta u = 0, \\ 2\left(f_x u + f_y v + f_t - \dfrac{1}{2}\alpha\Delta f\right) f_y - 2\cdot\dfrac{1}{2}\lambda\alpha\Delta v = 0. \end{cases} \tag{24}$$

With the approximations of Laplacians $\Delta u \approx \kappa(\bar{u}-u)$, $\Delta v \approx \kappa(\bar{v}-v)$, where $\bar{u}$, $\bar{v}$ denote the local averages and κ depends on the difference scheme, (24) can be expressed as the following equations:

$$\begin{cases} \left(f_x^2 + \dfrac{1}{2}\lambda\alpha\right)u + f_x f_y v = \dfrac{1}{2}\lambda\alpha\bar{u} + \dfrac{1}{2}\alpha f_x\Delta f - f_x f_t, \\ f_x f_y u + \left(f_y^2 + \dfrac{1}{2}\lambda\alpha\right)v = \dfrac{1}{2}\lambda\alpha\bar{v} + \dfrac{1}{2}\alpha f_y\Delta f - f_y f_t, \end{cases} \tag{25}$$

which can be solved by the Gauss-Seidel method or the Successive Over Relation (SOR) iteration. In our algorithm, by applying elimination method to (25), the velocity vector ω can be computed by the following iterative formulation:

$$\begin{cases} u^{k+1} = \bar{u}^k - \dfrac{f_x\bar{u}^k + f_y\bar{v}^k + f_t - \frac{1}{2}\alpha\Delta f}{\frac{1}{2}\lambda\alpha + f_x^2 + f_y^2} f_x, \\ v^{k+1} = \bar{v}^k - \dfrac{f_x\bar{u}^k + f_y\bar{v}^k + f_t - \frac{1}{2}\alpha\Delta f}{\frac{1}{2}\lambda\alpha + f_x^2 + f_y^2} f_y. \end{cases} \tag{26}$$

3.2 Estimation of diffusion factor

The most important parameter to estimate the large-scale velocity field, ω, is the diffusion factor α. Since α can be regarded as an unknown in the objective functional (22), one can compute α by cancelling the energy functional gradient with respect to this variable. Therefore, we have

$$\begin{aligned} \frac{\partial J}{\partial\alpha} = &\int_\Omega \left[-\Delta f\left(\partial_t f + \nabla f\cdot\omega - \frac{1}{2}\alpha\Delta f\right) - \beta^2|\nabla f|^2\right]\mathrm{d}\mathbf{x} \\ &+ \int_\Omega \frac{1}{2}\lambda \mid\nabla\omega\mid^2 \mathrm{d}\mathbf{x} = 0. \end{aligned} \tag{27}$$

Then we readily obtain

$$\hat{\alpha}^{k+1} = 2\frac{\int_\Omega \left[\Delta f\left(\nabla f\cdot\bar{\omega}^k + f_t\right) + \beta^2 \mid\nabla f\mid^2 - \frac{1}{2}\lambda \mid\nabla\bar{\omega}^k\mid^2\right]\mathrm{d}\mathbf{x}}{\int_\Omega (\Delta f)^2 \mathrm{d}\mathbf{x}},$$

(28)

where $\bar{\omega}^k$ is the estimated velocity vector from the previous iteration, defined by (26). An approximation of β is given in Appendix A.

3.3 Multi-resolution algorithm

For the basic optical flow methods, one common weakness is that the procedure can yield good results only when the magnitude of image motion is small (smaller than the shortest spatial wavelength present in the image (Heitz et al., 2010)). To overcome the estimation issue due to the large displacements, we use an incremental coarse-to-fine strategy. The main idea of this strategy can be divided into several processes: a) a multi-resolution representation through the successive Gaussian filtering and sub-sampling is applied to the images pair; b) the optical flow is computed from the coarse-resolution level and then projected onto the next finer level of the pyramid; in the projection step, image warping is required so we only need to compute the small velocity increments at the higher resolution level; c) this process is repeated at finer and finer spatial scales until the original image resolution is reached.

The choice of the image filtering process is significant for the multi-resolution algorithm. Gaussian filters are applied to the original images to reduce the noise effect. Furthermore, median filters are applied to the estimated velocity fields after each warping step for the purpose of eliminating the outliers, as proposed by Sun et al. (2010). The framework of the multi-resolution strategy is shown in Algorithm 1.

Algorithm 1: Multi-resolution algorithm with symmetric warping for motion estimation

Load image pair Img_1 **and** Img_2;
Pre-processing;
Pyramidal generation from level 0 (original) to L (coarsest);
Compute the weighting coefficient λ ;
for $l = L$ *to* 0 **do**
  if $l = L$ **then**
    Set initial velocities be 0 at coarsest level $\widehat{\omega_{l+1}} = 0$;
    Set initial estimation of α;
  else
    Expand the velocities from coarser level ω_{l+1} to finer level $\widehat{\omega_{l+1}}$ by interpolation;
  end
  for *Each warping step* **do**
    Symmetric warping
      $f_1 = warpForward(Img_1^l)$,
    $f_2 = warpInverse(Img_2^l)$.
    Optimization
      Compute the gradients and Laplacians f_t, ∇f, Δf;
      Compute the estimation of β^2;
      Estimate the motion field $\mathrm{d}\omega$ and α by iterations (26) and (28), respectively;
      Update $\omega_l = \widehat{\omega_{l+1}} + \mathrm{d}\omega$;
    Median filtering
  end
end
End multi-resolution;

4 Experimental Evaluation with Synthetic Data Sets

To investigate the performance of the proposed formulation, different synthetic image sequences are used in this section. The main advantage of testing on synthetic data sets is that the true velocity is known and can be used for comparison with the estimated motion field. Although these sequences are usually generated in ideal conditions, they are quite suitable for evaluating the performance of different approaches. A real experimental sequence is tested and discussed in the next section.

Hereafter, we follow a standard way to evaluate quantitatively the experimental results by computing the root mean square error (RMSE) over N pixels of the image:

$$RMSE = \sqrt{\frac{1}{N}\sum_{i=1}^{N}[(u_i^t - u_i^e)^2 + (v_i^t - v_i^e)^2]}, \tag{29}$$

where (u^t, v^t) and (u^e, v^e) denote the ground-truth velocity and the estimated velocity, respectively. The index i represents the pixel where optical flow is computed. RMSE is commonly used to validate the accuracy of the estimator in the literature. Therefore, we can also compare the proposed method with other optical flow approaches based on this criterion.

4.1 2D DNS turbulent flow

4.1.1 Data description

A synthetic sequence[1] with both particle and scalar images is provided by Carlier (2005) and generated by Direct Numerical Simulation (DNS). The phenomenon investigated is the spreading of a low diffusivity dye in a 2D homogeneous turbulent flow with Reynolds number $Re = 3000$ and Schmidt number $Sc = 0.7$. The intensity of the passive scalar images is proportional to the dye concentration. Both scalar sequence and particle sequence consist of 100 successive images at the resolution of 256×256 pixels. Figure 1

[1] Available online: `http://fluid.irisa.fr/`

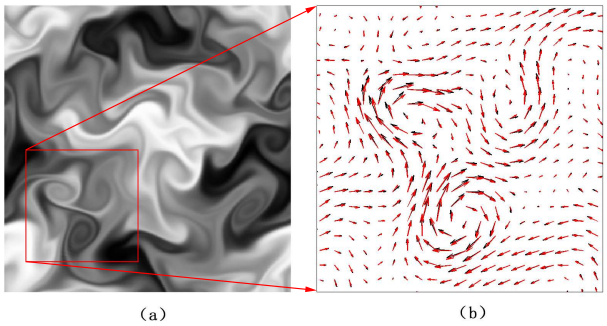

Fig. 3 Velocity vectors on DNS passive scalar image sequence at $t = 50$: (a) scalar image with zoomed area; (b) true velocity vectors (red) and the estimated vectors by the proposed method (black).

demonstrates a scalar image, a particle image and the corresponding vorticity map of this data set. The maximum displacement between two successive images is about 3.5 pixels. For both particle and scalar image sequences, a multi-resolution algorithm with 2 levels and 5 warping steps has been implemented.

4.1.2 Results

Scalar image sequence. The motion fields and vorticity maps estimated from different methods at time step $t = 50$ are illustrated in Figure 2. Here, the proposed technique is compared with the methods of Horn and Schunck (1981), Dérian et al. (2013), and Héas et al. (2012). We can observe from the vorticity maps that the proposed stochastic formulation performs better than the other references, especially in the area with high vorticity. The vortex structures are well recovered by the proposed optical flow formulation, whereas they are blurred by the HS method. Dérian et al. (2013) and Héas et al. (2012) achieve to estimate the large-scale structures of the flow. However, they fail to provide the small-scale components in some areas. Figure 3 illustrates the result of a typical area of the scalar image with a strong vortex. A zoom in this region shows that the estimated velocity field (black vectors) is highly consistent with the ground-truth (red vectors). This suggests that the novel optical flow under location uncertainty can provide a decent estimation of the flow velocity field.

Quantitative evaluations for the DNS passive scalar images are given in Figure 4. The RMSE errors of the proposed method and the HS method are plotted in Figure 4 (a). It can be seen that the accuracy of the new technique is drastically improved by more than 50% for the RMSE. Even compared with the state-of-the-art approaches, the proposed method shows the best performances. Error data of the other optical flow methods, including Yuan et al. (2007), Dérian et al. (2013), Héas et al. (2012), Kadri-Harouna et al. (2013), and Chen et al. (2015), are taken from Chen et al. (2015) and

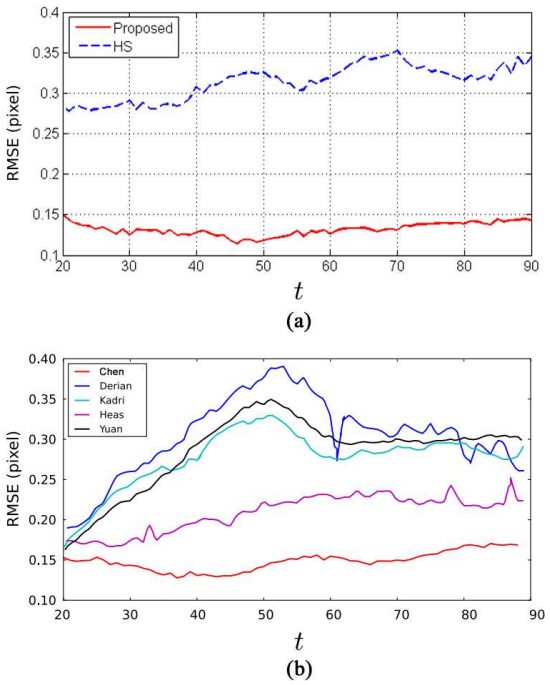

Fig. 4 RMSE errors of different estimators for DNS scalar image sequence. Results of the proposed method are plotted in figure (a), in comparison with the results of the HS method. The data of several state-of-the-art approaches, shown in figure (b), are extracted from Chen et al. (2015). (colored)

displayed in Figure 4 (b). The results of our method is close to (slightly better than) the results of Chen et al. (2015), which applies a data term based on the large eddy simulation (LES) sub-grid model and a divergence-free regularization term. Both the proposed technique and Chen et al. (2015) outperform the other methods for the whole passive scalar image sequence, indicating that the introduction of turbulence models is significant for fluid motion estimation. The method of Chen et al. (2015) depends on the standard deviation of a low-pass filtering applied on the sequence and on a regularization constant. Both constants are indeed difficult to fix in practice. The technique of Chen et al. (2015) depends also on the ratio of the Reynolds and Schmidt numbers which, though being exactly known here, is not always available with accuracy. The filtering standard deviation and the regularization must be adapted from one sequence to the other. On the contrary, the estimator under uncertainty proposed in this paper does not require such a tuning.

In Figure 5, we compare in particular the proposed method, the HS technique and the method of Héas et al. (2012). The proposed estimator can be seen as a parameter-free modification of the HS scheme with a new data model. And the method of Héas et al. (2012), similarly to the proposed one, also implements an estimation of the parameters involved in the regularization (by fitting of the second order statisti-

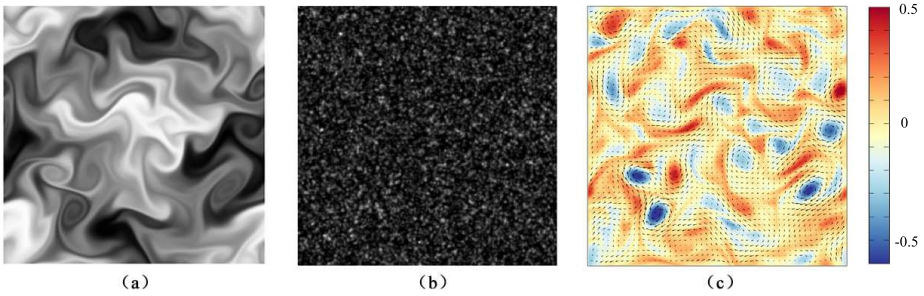

Fig. 1 Illustration of a sample frame ($t = 50$) from the DNS synthetic image sequence: (a) passive scalar image; (b) particle image; (c) vorticity map with the ground-truth velocity field.

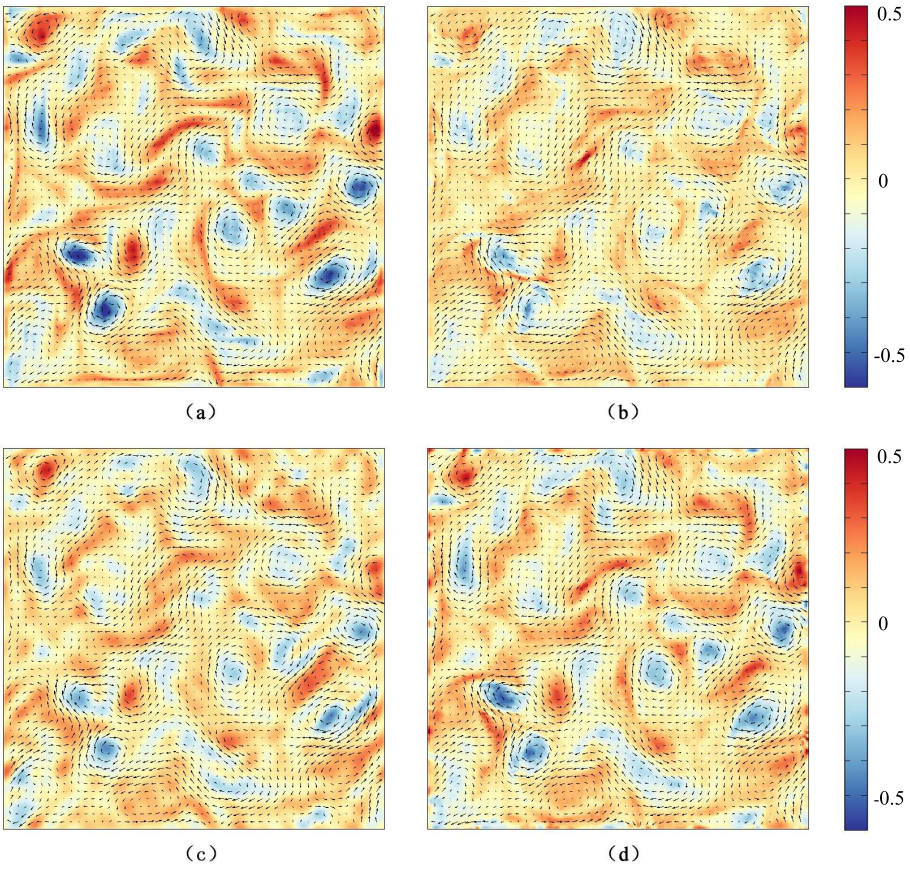

Fig. 2 Velocity fields and vorticity maps estimated from different methods on DNS passive scalar image sequence at $t = 50$: (a) proposed method; (b) Horn and Schunck (1981); (c) Dérian et al. (2013); (d) Héas et al. (2012).

cal moment of the flow velocity increments to a power law function). The energy spectra of these estimations are plotted in Figure 5. We can observe that at large scales the proposed solution is much closer to the DNS spectrum. The inertial range (with a spectrum slope close to -5, which is reasonable for a 2D turbulence in presence of friction) is also clearly extended with a much finer cutoff (at 6-7 pixels for the proposed technique against 15-20 pixels for the HS method and Héas et al. (2012)).

In Figure 5 we plot also the energy and enstrophy fluxes across scales, denoted as respectively, $\Pi(k)$ and $Z(k)$. We refer to Boffetta and Ecke (2012) for the computation of those terms and the general insights on 2D turbulence. It can be observed that the proposed technique achieves to reproduce the inverse energy cascade (i.e., negative energy flux at large

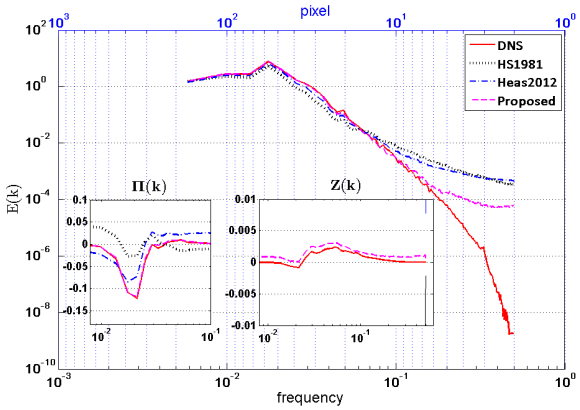

Fig. 5 Spectrum analysis of the turbulent velocity for DNS scalar image sequence. $E(k)$ denotes the energy at a given frequency, $\Pi(k)$ and $Z(k)$ the energy flux and enstrophy flux, respectively. For clarity reasons the enstrophy fluxes of Héas et al. (2012) and HS method are not shown. They are almost constant and very badly recovered with a value of 0.17 and -0.08 for Héas et al. (2012) and HS method, respectively.

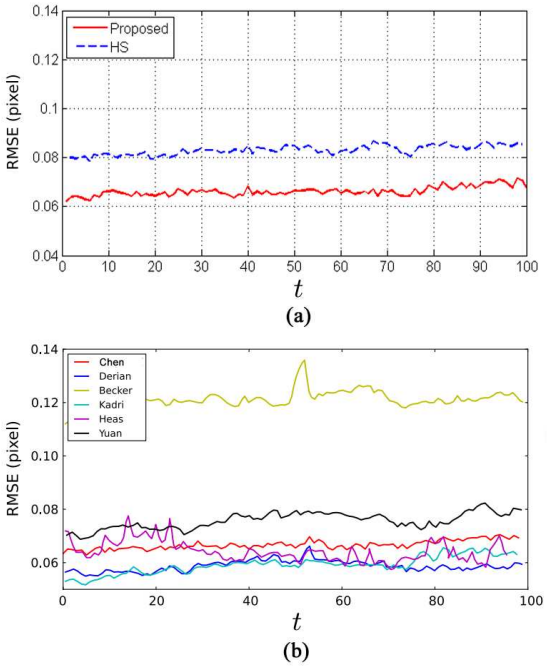

Fig. 6 RMSE errors of different estimators for DNS particle image sequence. Results of the proposed method are plotted in figure (a), in comparison with the results of the HS method. The data of several state-of-the-art approaches, shown in figure (b), are extracted from Chen et al. (2015). (colored)

scale), which is consistent with the physical solution reported in Boffetta and Ecke (2012). In the inertial subrange, the model under uncertainty is associated to a null energy flux and a positive enstrophy flux associated to the direct enstrophy cascade. Those fluxes are very close to those of the reference DNS. In comparison, the model of Héas et al. (2012), though providing a negative energy flux at large scale as well, is associated to an erroneous positive energy flux in the inertial enstrophy cascade subrange together with a much too strong positive enstrophy flux (with a constant value almost two orders larger than the reference). As for the HS technique, it shows a negative enstrophy flux in the direct enstrophy cascade subrange. Hence, those two techniques provide solutions that do not correspond to the physics of 2D turbulence. The model under uncertainty demonstrates on this example its ability to estimate a physical solution.

Particle image sequence. In general, particle images are highly textured (namely the gradient of the image intensity has a high amplitude), hence they are more suitable for motion estimation than scalar images. Therefore, even the classical HS method can provide satisfactory estimation for DNS particle image sequence. The RMSE curves of different estimators for DNS particle image sequence are illustrated in Figure 6. As shown in Figure 6 (a), the proposed formulation performs better than the HS method again. However, the improvement is not as significant as that for scalar images. Compared to the results shown in Figure 6 (b), the proposed formulation also outperforms some of the state-of-the-art approaches, such as Becker et al. (2012) and Yuan et al. (2007). The methods of Dérian et al. (2013) and Kadri-Harouna et al. (2013) which use higher-order regularizer provide best results in this case. It can be seen that the gap between these methods and the proposed formulation is however comparatively small. In addition, the particle density does not allow to capture well in that case the small-scale variation of the luminance. Nevertheless, it must be recalled that contrary to the other techniques, the proposed estimator does not require a precise tuning of the smoothing constant. The level of accuracy obtained by this parameter-free method is therefore a very good illustration of robustness.

Similar conclusion can be drawn from Figure 7, which shows the spectra of the velocity fields estimated from DNS particle images for the same methods as in the scalar sequence (namely the HS method, Héas et al. (2012) and the proposed estimator). The different estimators, including the HS method, all produce energy spectra that are very close to the reference DNS spectrum at large scales. A cutoff at about 8 pixels for the proposed technique can be observed. This cutoff remains thus of the same order as in the scalar case. As clearly seen from the figure, the proposed method performs much better than the HS method at small scales. The spectrum recovered by our parameter-free estimator is similar to the spectrum obtained by the method of Héas et al. (2012), which depends in a very sensitive way on the two estimated parameters involved in the power law regularization (e.g., the power spectrum slope and the dissipation rate). This high sensitivity can be appreciated from the instabilities of the RMSE curve along time, which are shown in Figure 6 (b).

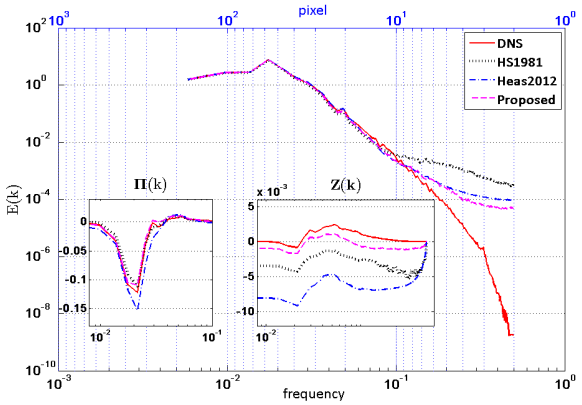

Fig. 7 Spectrum analysis of the turbulent velocity for DNS particle image sequence. $E(k)$ denotes the energy at a given frequency, $\Pi(k)$ and $Z(k)$ the energy flux and enstrophy flux, respectively.

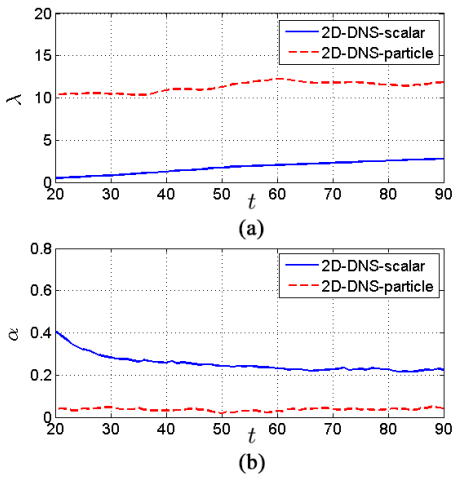

Fig. 8 Estimated parameters λ and α for DNS scalar and particle image sequences.

As in the scalar case, the energy and enstrophy fluxes are much better recovered by the proposed estimator. The approach under uncertainty is the only one that allows restoring a direct enstrophy cascade (positive enstrophy fluxes in the inertial range). The methods of HS and Héas et al. (2012) are associated to an erroneous strong negative value of the enstrophy flux, signature of an enstrophy cascade in the wrong direction across all the scales. The three methods are all associated to a negative energy flux at large scale and a null energy flux in the inertial subrange; the three detect thus an inverse energy cascade. The proposed method and the HS technique have an energy flux that is however closer to the reference than the one estimated by the technique of Héas et al. (2012). This latter shows in particular a high sensitivity to the data (for the same flow of reference the technique goes from a strong positive enstrophy flux for the scalar sequence to a strong negative enstrophy flux for the particle images). The HS estimator does not show this inconsistancy. As in the previous case, only the estimator under uncertainty provides solutions that are in accordance with the physics of 2D turbulence. Compared to the scalar image, the estimator under uncertainty, provides a slight underestimation of the enstrophy flux. This is likely due to a less good estimation of the small-scale velocity action for the sparse particle images.

Parameters estimation. Let us examine the estimated parameters λ and α, which are given by (20) and (28), respectively. Figure 8 shows the values of λ and α estimated from the 2D DNS image sequences. As we can see, the parameter-free formulation proposed in this paper provides robust estimations of the parameters. Note that λ is fixed on the sole basis of a dimensional consideration. Compared to the weighting coefficients used by Chen et al. (2015), the estimated values of λ are relatively small. However, it does not affect the result too much.

In summary, we see from these synthetic sequences that the optical flow formulation under location uncertainty can achieve to estimate good results for 2D DNS turbulent flow images, whether in the scalar case or in the particle case.

4.2 SQG data set

4.2.1 Data description

This synthetic data set is obtained from a Surface Quasi-Geostrophic (SQG) model[2]. The chosen configuration represents an idealized oceanic domain of 1000×1000 km with periodic boundary conditions. The corresponding 256×256 pixels grid is initialized with random buoyancy fluctuations for which the power spectral density follows a -5/3 power-law. The simulation is then carried out over 21 days of physical time, with a 12-s numerical time-step. Images of the buoyancy and the ground-truth velocity fields are saved every hour. The largest apparent displacements between two successive frames are of the order of 7 pixels. A sample frame and the reference vorticity map from the synthetic SQG sequence are illustrated in Figure 9. It can be noticed that the image exhibits large areas with poor photometric gradients. It constitutes thus a difficult case as it associates long range displacements and low photometric gradients.

The SQG sequence contains over 500 successive frames as well as the corresponding reference velocities. For simplicity, the validation of SQG sequence is only done at every 50 time steps (namely $t = 50, 100, \cdots, 450, 500$). The estimated motion field is extracted from image n and image $n+1$, and evaluated with the ground-truth. A multi-

[2] Available online: `https://github.com/vressegu/sqgmu`

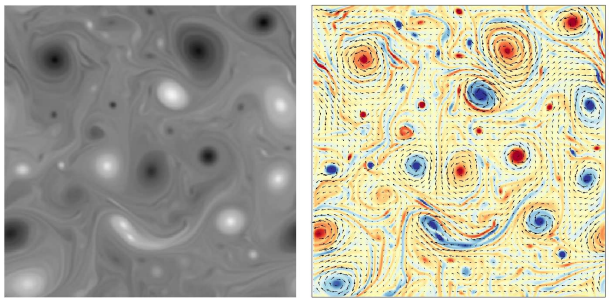

(a) (b)

Fig. 9 Illustration of a sample frame ($t = 450$) from the synthetic SQG sequence: (a) passive scalar image; (b) the simulated ground-truth velocity field with vorticity map, which is used for evaluation of the estimated motion hereafter.

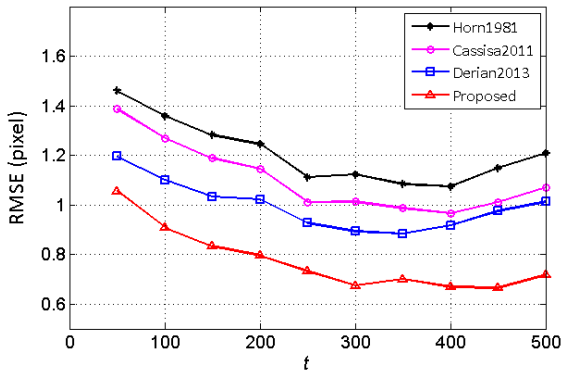

Fig. 10 RMSE errors for SQG scalar image sequence.

resolution algorithm with 2 levels and 2 warping steps has been implemented.

4.2.2 Results

Figure 10 compares the results in terms of RMSE of the proposed method to those of three other estimators (Horn and Schunck, 1981; Cassisa et al., 2011; Dérian et al., 2013). The best weighting coefficients were selected properly for each method except for the proposed formulation (the values of λ and α are about 0.3 and 0.25, respectively). As mentioned above, this sequence constitutes a difficult benchmark for motion estimation. Therefore, one can notice that the estimation errors for the SQG sequence are much larger than those associated to the DNS sequence. As seen in Figure 10, the proposed method clearly outperforms the other estimators. Compared to the HS method, the proposed formulation improves the accuracy significantly by about 40%. The methods of Cassisa et al. (2011) and Dérian et al. (2013) both succeed to improve the results of the HS estimator but not to the same extent as the estimator under uncertainty.

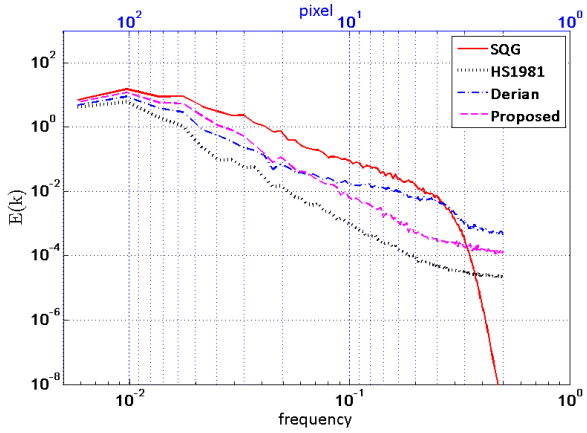

Fig. 12 Spectrum analysis of the turbulent velocity for SQG scalar image sequence.

To observe more details, an example of the estimated vorticity maps on the SQG sequence is illustrated in Figure 11. Once again, the HS method is unable to extract the vortex flow correctly as it yields an over-smoothing of the flow velocity fields. On the contrary, the stochastic optical flow technique provides estimates with clear turbulence patterns, which is more consistent with the large-scale motion field of the ground-truth. The multi-scale wavelet approach (Dérian et al., 2013), being more sensitive at fine scales, is able to retrieve thin structures such as filaments which correspond to the apparent displacement of fronts (high photometric gradients). However, due to the 1-hour time-step between two frames, these fine scale displacements do not necessarily match with the true instantaneous velocity field, as such fine structures evolve rapidly. Moreover, the large scale vortices in Figure 11 (b) are not as well retrieved as those in Figure 11 (c).

This is also confirmed by the spectrum analysis, as shown in Figure 12. The proposed solution is closer to the SQG spectrum at the scales larger than 12 pixels. The method of Dérian et al. (2013) recovers more energy at the small scales. However, it is associated to a flat spectrum, which is likely to be the signature of the strong vorticity noise visible in Figure 11 (b).

5 Experiment on Real Images

An experimental image sequence of 2D turbulence which can be used to investigate the performance of fluid motion estimators is provided by Jullien et al. (2000). The authors presented the first detailed experimental observation of the Batchelor regime (Batchelor, 1959), in which a scalar was dispersed by a large-scale strain, at high Péclet numbers up to 10^7. The Batchelor regime was observed in a controlled two-dimensional turbulent flow. A CCD camera was used

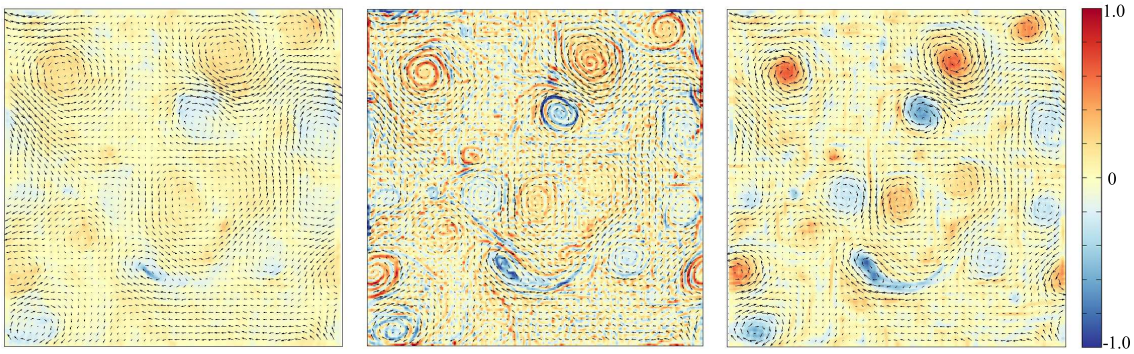

Fig. 11 Results at $t = 450$ on the synthetic SQG scalar image sequence: (a) estimated velocity field and vorticity map from the HS method; (b) estimated velocity field and vorticity map from Dérian et al. (2013); (c) estimated velocity field and vorticity map from the proposed method.

to visualize the scalar concentration field. For more experimental details, we refer to Jullien et al. (2000).

The recorded experimental sequence is composed of over 90 scalar images at the resolution of 512×512 pixels. Two successive frames of this sequence are displayed in Figure 13 (a) and (b), respectively. As the observation is forced at large scale, there are few sub-grid velocity components in this case. However, it is still difficult to estimate the velocity field from these images due to strong turbulent vortices. The maximum velocity magnitude for this sequence is about 15 pixels per frame. To cope with large displacement, we implement a multi-resolution algorithm with 5 levels and 2 warping steps. Furthermore, the estimated motion fields are projected into a divergence-free space at the end of the estimation process. For the parameters estimation, the values of λ and α are around 0.1 and 1, respectively.

Since the correct velocity fields are not available for this real experiment, evaluation criteria such as RMSE introduced above cannot be used. However, the estimated results can be compared based on their vorticity. Figure 13 (c), (d) demonstrate the vorticity maps estimated from the HS method and the proposed method. It can be seen that the result of the HS method is over-smoothed, while the result of the proposed formulation shows more finer structures on the vorticity map. Furthermore, a spectrum analysis of the velocity fields is illustrated in Figure 14. As we can see, the spectrum slope of the proposed formulation is close to $-5/3$ at the large scales and -5 at the small scales. However, the HS method produces a flat spectrum curve which is not consistent with the property of 2D turbulent flow. This fact is confirmed by inspecting the energy and enstrophy fluxes. The $-5/3$ region is associated to a negative energy flux in both cases (with a stronger negative flux for the model under uncertainty). A direct enstrophy cascade (positive enstrophy flux) is well recovered by the proposed method in the region corresponding to a -5 slope spectrum. The HS estimator shows a physically erroneous constant negative enstrophy flux on an extended scale range.

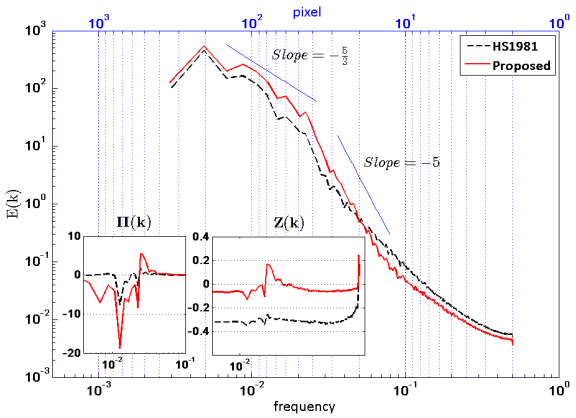

Fig. 14 Spectrum analysis of the turbulent velocity for experimental scalar images. $E(k)$ denotes the energy at a given frequency, $\Pi(k)$ and $Z(k)$ the energy flux and enstrophy flux, respectively.

Considering the stochastic transport equation in the optical flow formulation enables to take into account the small-scale unresolved components of the velocity field. Therefore, small energetic vortices can be detected. As quality criteria, the vorticity maps and the spectra of this experimental scalar image sequence indicate once again the efficiency of the proposed technique.

6 Conclusion

In this paper, we introduce a novel optical flow formulation build from the principles of the modeling under location uncertainty (Mémin, 2014). This motion estimator is designed to take into account the action on the estimated motion field of the unresolved small-scale motion component. Such a modeling allows us to interpret the tradition-

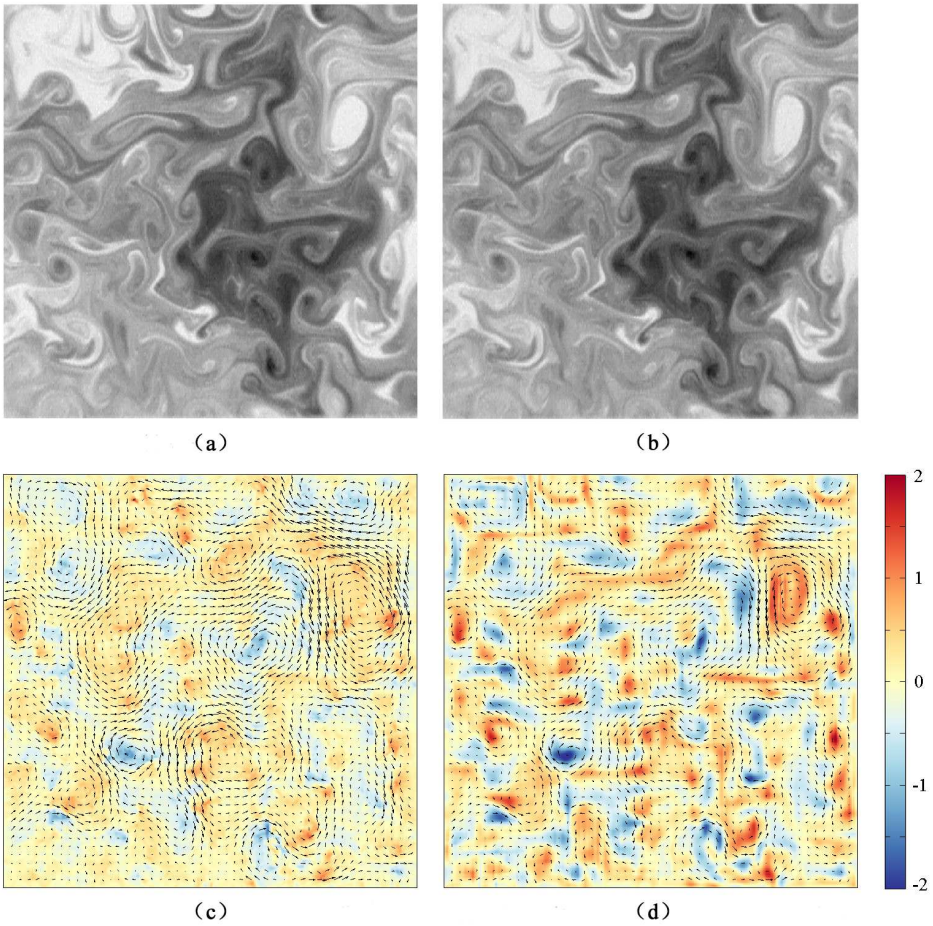

Fig. 13 Results on experimental scalar images: (a) first frame; (b) second frame; (c) estimated velocity field and vorticity map from the HS method; (d) estimated velocity field and vorticity map from the proposed method.

al smoothing functions as isotropic turbulence models and to correct accordingly the optical flow constraint equation when a scalar transported by a turbulent flow is considered. The estimator is formalized as the minimizer of an energy functional, similarly to most of the dense optical flow methods. However, a stochastic flow representation is considered in the formulation. The small-scale component of the turbulent velocity enters into the optical flow constraint equation through a transport equation established from a stochastic formulation of the Reynolds transport theorem. The whole data term of the proposed optical flow formulation is subsequently obtained from the variance of the stochastic transport operator, while the regularization term is derived within the same stochastic context from the assumption of constant kinetic energy. This formulation corresponds finally to an extension of a classical dense motion estimator in which a turbulence flow model is introduced. This novel formulation allows us to estimate explicitly the different parameters involved. This contrasts strongly with the manual parameter tuning associated to most of the motion estimators proposed so far.

The corresponding parameter-free estimator provides very good results on experimental and synthetic image sequences of passive scalar. It significantly outperforms the results of other state-of-the-art approaches for their best choice of parameter values. Small-scale turbulent structures are clearly detected by the proposed optical flow formulation. The new optical flow formulation, whose implementation remains simple and close to the original Horn and Schunck estimator, constitutes a very promising technique for the estimation of turbulent flow velocity fields.

There are some possible extensions of the proposed formulation that can be investigated in the future. Although the stochastic transport equation in this paper is limited to a 2D domain, it can be easily extended to the three-dimensional (3D) case, by introducing the third component: $\mathbf{x} = (x, y, z)^T$ and $\boldsymbol{\omega} = (u, v, w)^T$. Then we can have the 3D material derivative which is identical to (11), followed by the same derivations in Section 2.1. To this end, an objective functional with

respect to the 3D velocity field is obtained, where the variance factor $\boldsymbol{a}$ is now a 3×3 matrix and an additional regularizer for the third velocity component is added to the regularization term. Such a formulation for motion estimation from 3D images is similar to the one proposed by Su and Dahm (1996), which applied an integral minimization technique based on the standard transport equation rather than using the matching techniques as developed in Tokumaru and Dimotakis (1995) and Deusch et al. (2000). However, the introduction of stochastic representation in this paper may help to improve the accuracy of estimation for 3D turbulent flow.

In addition, although we have evaluated our method on different kinds of fluid images (i.e. particle images, scalar images and sea surface temperature images), it can be further tested in other areas of flow analysis, such as extracting the displacements from background oriented schlieren images (Atcheson et al., 2009) or skin-friction fields from surface flow visualizations (Liu, 2013). For instance, Liu (2013) established the quantitative relationships between a skin-friction field and the measured relevant physical quantities (e.g., oil-film, surface temperature and species concentration). Therefore, the variational formulation for determining the optical flow can be adopted. It is obviously possible to introduce the random component into the motion field in this framework and derive the stochastic representation of these equations, as the idea presented in Resseguier et al. (2017b). The suitability of the proposed algorithm for various applications is worth investigating.

A Variance of Stochastic Transport Operator

Before deriving the variance of the stochastic transport operator, we first recall briefly the notions of quadratic variation and covariation, which are important in stochastic calculus. Suppose that X_t, Y_t are stochastic processes defined on the probability space $(\Omega,\mathscr{F},\mathbb{P})$, the quadratic covariation process denoted as $\langle X,Y\rangle_t$, is defined as the limit in probability:

$$\langle X,Y\rangle_t = \lim_{\delta t_i\to 0}\sum_{i=0}^{n-1}\left(X_{t_{i+1}}-X_{t_i}\right)\left(Y_{t_{i+1}}-Y_{t_i}\right)^T, \tag{30}$$

with $t_1<t_2<\cdots<t_n$ and $\delta t_i = t_{i+1}-t_i$. For the Brownian motion, the quadratic covariances can be computed by the following rules:

$$\begin{cases}\langle B,B\rangle_t = t,\\ \langle B,h\rangle_t = \langle h,B\rangle_t = \langle h,h\rangle_t = 0,\end{cases} \tag{31}$$

where h is a deterministic function and B denotes a Brownian process. Now we can recall the stochastic transport of a scalar f and its expectation, i.e.,

$$\mathbb{D}_t f = \mathrm{d}_t f + \left[\nabla f\cdot\omega^* - \tfrac{1}{2}\nabla\cdot(\boldsymbol{a}\nabla f)\right]\mathrm{d}t + \nabla f\cdot\sigma\mathrm{d}\mathbf{B}_t, \tag{32}$$

$$\mathbb{E}(\mathbb{D}_t f) = \left[\partial_t\mathbb{E}(f) + \nabla\mathbb{E}(f)\cdot\omega^* - \tfrac{1}{2}\nabla\cdot(\boldsymbol{a}\nabla\mathbb{E}(f))\right]\mathrm{d}t. \tag{33}$$

Assuming a stationary distribution, then the expectation is the solution of a stationary equation and $\mathbb{E}(\mathbb{D}_t f)=0$. Therefore, the variance of the stochastic transport operator is expressed as:

$$\begin{aligned}Var(\mathbb{D}_t f) =& \mathbb{E}\left[(\mathbb{D}_t f-\mathbb{E}(\mathbb{D}_t f))^2\right] = \mathbb{E}\left[(\mathbb{D}_t f)^2\right]\\ =& \mathbb{E}\left\{\left[\mathrm{d}_t f + \left(\nabla f\cdot\omega^* - \frac{1}{2}\nabla\cdot(\boldsymbol{a}\nabla f)\right)\mathrm{d}t\right]^2\right\}\\ &+\mathbb{E}\left\{(\nabla f\cdot\sigma\mathrm{d}\mathbf{B}_t)^2\right\}\\ &+\mathbb{E}\left\{2\left(\mathrm{d}_t f+\nabla f\cdot\omega^* - \frac{1}{2}\nabla\cdot(\boldsymbol{a}\nabla f)\right)(\nabla f\cdot\sigma\mathrm{d}\mathbf{B}_t)\right\},\end{aligned} \tag{34}$$

where the second term and the third term involve a Brownian term. According to the Itô isometry, we obtain:

$$\begin{aligned}\mathbb{E}\left\{(\nabla f\cdot\sigma\mathrm{d}\mathbf{B}_t)^2\right\} &= \mathbb{E}\left\{\langle\nabla f\cdot\sigma\mathrm{d}\mathbf{B}_t,\ \nabla f\cdot\sigma\mathrm{d}\mathbf{B}_t\rangle\right\}\\ &= \mathbb{E}\left\{\left[(\nabla f)^T\boldsymbol{a}(\nabla f)\right]\mathrm{d}t\right\}\end{aligned} \tag{35}$$

and

$$\begin{aligned}&\mathbb{E}\left\{2\left(\mathrm{d}_t f+\nabla f\cdot\omega^* - \frac{1}{2}\nabla\cdot(\boldsymbol{a}\nabla f)\right)(\nabla f\cdot\sigma\mathrm{d}\mathbf{B}_t)\right\}\\ =&2\mathbb{E}\left\{\left\langle\mathrm{d}_t f+\nabla f\cdot\omega^* - \frac{1}{2}\nabla\cdot(\boldsymbol{a}\nabla f),\ \nabla f\cdot\sigma\mathrm{d}\mathbf{B}_t\right\rangle\right\}\\ =&2\mathbb{E}\left\{\langle\mathrm{d}_t f,\ \nabla f\cdot\sigma\mathrm{d}\mathbf{B}_t\rangle\right\},\end{aligned} \tag{36}$$

where (36) represents the correlation between the martingale part of $\mathrm{d}_t f$ and the random advection term $\nabla f\cdot\sigma\mathrm{d}\mathbf{B}_t$. For a conserved quantity f, we have the transport equation $D_t f = \mathbb{D}_t f = 0$. This implies that when separating $f=\tilde{f}+f'$ in terms of its bounded variation part and its martingale part (i.e., time scale separation in terms of $\mathrm{d}t$ and $\mathrm{d}\mathbf{B}_t$, which is a unique decomposition), the transport equation can be separated into:

$$\begin{cases}\dfrac{\partial\tilde{f}}{\partial t}\mathrm{d}_t + \left[\nabla f\cdot\omega^* - \dfrac{1}{2}\nabla\cdot(\boldsymbol{a}\nabla f)\right]\mathrm{d}t = 0,\\ \mathrm{d}_t f' + \nabla f\cdot\sigma\mathrm{d}\mathbf{B}_t = 0.\end{cases} \tag{37}$$

Thus, we have

$$\begin{aligned}0 &= \left\langle\mathrm{d}_t f' + \nabla f\cdot\sigma\mathrm{d}\mathbf{B}_t,\ \mathrm{d}_t f' + \nabla f\cdot\sigma\mathrm{d}\mathbf{B}_t\right\rangle,\\ &= \left\langle\mathrm{d}_t f',\ \mathrm{d}_t f'\right\rangle + \left\langle\nabla f\cdot\sigma\mathrm{d}\mathbf{B}_t,\ \nabla f\cdot\sigma\mathrm{d}\mathbf{B}_t\right\rangle + 2\left\langle\mathrm{d}_t f',\ \nabla f\cdot\sigma\mathrm{d}\mathbf{B}_t\right\rangle.\end{aligned} \tag{38}$$

Note that $\langle\mathrm{d}_t f',\ \mathrm{d}_t f'\rangle = \langle\mathrm{d}_t f,\ \mathrm{d}_t f\rangle$, since the quadratic variation of bounded variation functions (such as the deterministic functions) is equal to 0. Equation (37) shows that in the case of a transported quantity $\mathrm{d}_t f' = -\nabla f\cdot\sigma\mathrm{d}\mathbf{B}_t$. When the conservation does hold only approximately (as in the case of the brightness consistency assumption), we will assume the proportionality relation: $\mathrm{d}_t f' = \beta\nabla f\cdot\sigma\mathrm{d}\mathbf{B}_t$, where β has to be fixed or estimated (note that $\beta=-1$ for a strict stochastic transport). This assumption comes to assume that the highly fluctuating part of the intensity difference is explained by the transport of the luminance function by the small-scale motion up to a proportionality factor. With this assumption we have:

$$\begin{aligned}\mathbb{E}\left\{\left\langle\mathrm{d}_t f',\ \mathrm{d}_t f'\right\rangle\right\} &= \mathbb{E}\left\{\left\langle\beta\nabla f\cdot\sigma\mathrm{d}\mathbf{B}_t,\ \beta\nabla f\cdot\sigma\mathrm{d}\mathbf{B}_t\right\rangle\right\}\\ &= \beta^2\mathbb{E}\left\{\left[(\nabla f)^T\boldsymbol{a}(\nabla f)\right]\mathrm{d}t\right\}.\end{aligned} \tag{39}$$

An estimate of β from this equation can be readily obtained:

$$\beta^2 = \mathbb{E}\left[\frac{(\mathrm{d}_t f')^2}{(\nabla f)^T\boldsymbol{a}(\nabla f)}\right]. \tag{40}$$

In practice the fluctuation $f' = f - \tilde{f}$ is set as the difference between the luminance function and a local (spatial/temporal) mean $\bar{f}$. For successive images, the temporal difference is thus $\mathrm{d}_t f' = f_2' - f_1' = (f_2 - \bar{f}_2) - (f_1 - \bar{f}_1)$. Note that as $\boldsymbol{a}$ is also an unknown in the optical flow formulation. This leads to an interleaved optimization problem. Here we adopt a simpler strategy in which the proportionality coefficient is fixed from the value of $\boldsymbol{a}$ at the previous multi-resolution level (i.e., $\boldsymbol{a}^{L-1}$).

Eventually, by combining (38), (39) and (35), it yields

$$\begin{aligned} 2\mathbb{E}\left\{\left\langle \mathrm{d}_t f',\, \nabla f \cdot \sigma \mathrm{d}\mathbf{B}_t \right\rangle\right\} = &- \mathbb{E}\left\{\left[(\nabla f)^T \boldsymbol{a}(\nabla f)\right] \mathrm{d}t\right\} \\ &- \beta^2 \mathbb{E}\left\{\left[(\nabla f)^T \boldsymbol{a}(\nabla f)\right] \mathrm{d}t\right\}. \end{aligned} \tag{41}$$

Substituting these equations into (34), we finally obtain:

$$\begin{aligned} Var(\mathbb{D}_t f) = &\mathbb{E}\left\{\left[\mathrm{d}_t f + \left(\nabla f \cdot \omega^* - \frac{1}{2}\nabla \cdot (\boldsymbol{a}\nabla f)\right)\mathrm{d}t\right]^2\right\} \\ &- \mathbb{E}\left\{\beta^2 \left[(\nabla f)^T \boldsymbol{a}(\nabla f)\right] \mathrm{d}t\right\}. \end{aligned} \tag{42}$$

A minimum variance estimator with a spatial averaging for the expectation or considering a homogeneous Gaussian density leads to minimize:

$$\begin{aligned} Var(\mathbb{D}_t f) = &\int_\Omega \left[\mathrm{d}_t f + \left(\nabla f \cdot \omega^* - \frac{1}{2}\nabla \cdot (\boldsymbol{a}\nabla f)\right)\mathrm{d}t\right]^2 \mathrm{d}\mathbf{x} \\ &- \int_\Omega \beta^2 \left[(\nabla f)^T \boldsymbol{a}(\nabla f)\mathrm{d}t\right] \mathrm{d}\mathbf{x}. \end{aligned} \tag{43}$$

References

Atcheson, B., Heidrich, W., and Ihrke, I. (2009). An evaluation of optical flow algorithms for background oriented schlieren imaging. *Experiments in fluids*, 46(3):467–476.

Batchelor, G. (1959). Small-scale variation of convected quantities like temperature in turbulent fluid. *Journal of Fluid Mechanics*, 5(01):113–133.

Becker, F., Wieneke, B., Petra, S., Schroder, A., and Schnorr, C. (2012). Variational adaptive correlation method for flow estimation. *IEEE Transactions on Image Processing*, 21(6):3053–3065.

Beyou, S., Cuzol, A., Gorthi, S., and Mémin, E. (2013). Weighted ensemble transform kalman filter for image assimilation. *Tellus A: Dynamic Meteorology and Oceanography*, 65(18803).

Black, M. and Anandan, P. (1996). The robust estimation of multiple motions: Parametric and piecewise-smooth flow fields. *Computer Vision and Image Understanding*, 63(1):75–104.

Boffetta, G. and Ecke, R. (2012). Two-dimensional turbulence. *Annual Review of Fluid Mechanics*, 44:427–451.

Brox, T., Bruhn, A., Papenberg, N., and Weickert, J. (2004). High accuracy optical flow estimation based on a theory for warping. In *Proceedings of the European Conference on Computer Vision*, pages 25–36.

Bruhn, A., Weickert, J., and Schnörr, C. (2005). Lucas/Kanade meets Horn/Schunck: Combining local and global optic flow methods. *International Journal of Computer Vision*, 61(3):211–231.

Carlier, J. (2005). Second set of fluid mechanics image sequences. *European Project Fluid Image Analysis and Description (FLUID) - http://www.fluid.irisa.fr*.

Cassisa, C., Simoens, S., Prinet, V., and Shao, L. (2011). Subgrid scale formulation of optical flow for the study of turbulent flow. *Experiments in Fluids*, 51(6):1739–1754.

Chen, X., Zillé, P., Shao, L., and Corpetti, T. (2015). Optical flow for incompressible turbulence motion estimation. *Experiments in Fluids*, 56(1):1–14.

Corpetti, T., Heitz, D., Arroyo, G., Mémin, E., and Santa-Cruz, A. (2006). Fluid experimental flow estimation based on an optical-flow scheme. *Experiments in Fluids*, 40(1):80–97.

Corpetti, T., Mémin, E., and Pérez, P. (2002). Dense estimation of fluid flows. *IEEE Transactions on Pattern Analysis and Machine Intelligence*, 24(3):365–380.

Crisan, D., Flandoli, F., and Holm, D. (2017). Solution properties of a 3D stochastic Euler fluid equation. *arXiv preprint arXiv:1704.06989*.

Cuzol, A. and Mémin, E. (2009). A stochastic filtering technique for fluid flow velocity fields tracking. *IEEE Transactions on Pattern Analysis and Machine Intelligence*, 31(7):1278–1293.

Dérian, P., Héas, P., Herzet, C., and Mémin, E. (2013). Wavelets and optical flow motion estimation. *Numerical Mathematics: Theory, Methods and Applications*, 6(1):116–137.

Deusch, S., Merava, H., Dracos, T., and Rys, P. (2000). Measurement of velocity and velocity derivatives based on pattern tracking in 3D LIF images. *Experiments in fluids*, 29(4):388–401.

Héas, P., Mémin, E., Heitz, D., and Mininni, P. (2012). Power laws and inverse motion modeling: application to turbulence measurements from satellite images. *Tellus A: Dynamic Meteorology and Oceanography*, 64(10962).

Heitz, D., Héas, P., Mémin, E., and Carlier, J. (2008). Dynamic consistent correlation-variational approach for robust optical flow estimation. *Experiments in Fluids*, 45(4):595–608.

Heitz, D., Mémin, E., and Schnörr, C. (2010). Variational fluid flow measurements from image sequences: synopsis and perspectives. *Experiments in Fluids*, 48(3):369–393.

Holm, D. (2015). Variational principles for stochastic fluid dynamics. In *Proc. R. Soc. A*, volume 471, page 20140963. The Royal Society.

Horn, B. and Schunck, B. (1981). Determining optical flow. *Artificial Intelligence*, 17(1-3):185–203.

Jullien, M., Castiglione, P., and Tabeling, P. (2000). Experimental observation of Batchelor dispersion of passive tracers. *Physical Review Letters*, 85(17):3636.

Kadri-Harouna, S., Dérian, P., Héas, P., and Mémin, E. (2013). Divergence-free wavelets and high order regularization. *International Journal of Computer Vision*, 103(1):80–99.

Kadri-Harouna, S. and Mémin, E. (2017). Stochastic representation of the reynolds transport theorem: revisiting large-scale modeling. *Computers & Fluids*, 156:456–469.

Lilly, K. (1966). On the application of the eddy viscosity concept in the inertial subrange of turbulence. Technical Report 123, NCAR.

Liu, T. (2013). Extraction of skin-friction fields from surface flow visualizations as an inverse problem. *Measurement Science and Technology*, 24(12):124004.

Liu, T., Merat, A., Makhmalbaf, H., Fajardo, C., and Merati, P. (2015). Comparison between optical flow and cross-correlation methods for extraction of velocity fields from particle images. *Experiments in Fluids*, 56(8):166.

Liu, T. and Shen, L. (2008). Fluid flow and optical flow. *Journal of Fluid Mechanics*, 614:253–291.

Mémin, E. (2014). Fluid flow dynamics under location uncertainty. *Geophysical & Astrophysical Fluid Dynamics*, 108(2):119–146.

Mémin, E. and Pérez, P. (1998). Dense estimation and object-based segmentation of the optical flow with robust techniques. *IEEE Transactions on Image Processing*, 7(5):703–719.

Papadakis, N. and Mémin, E. (2008). Variational assimilation of fluid motion from image sequence. *SIAM Journal on Imaging Sciences*, 1(4):343–363.

Papadakis, N., Mémin, E., Cuzol, A., and Gengembre, N. (2010). Data assimilation with the weighted ensemble Kalman filter. *Tellus A*, 62(5):673–697.

Quénot, G., Pakleza, J., and Kowalewski, T. (1998). Particle image velocimetry with optical flow. *Experiments in Fluids*, 25(3):177–189.

Raffel, M., Willert, C., Wereley, S., and Kompenhans, J. (2007). *Particle Image Velocimetry: A Practical Guide*. Springer.

Resseguier, V., Mémin, E., and Chapron, B. (2017a). Geophysical flows under location uncertainty, Part I: Random transport and general models. *Geophysical & Astrophysical Fluid Dynamics*, 111(3):149–176.

Resseguier, V., Mémin, E., and Chapron, B. (2017b). Geophysical flows under location uncertainty, Part II: Quasigeostrophic models and efficient ensemble spreading. *Geophysical & Astrophysical Fluid Dynamics*, 111(3):177–208.

Resseguier, V., Mémin, E., and Chapron, B. (2017c). Geophysical flows under location uncertainty, Part III: SQG and frontal dynamics under strong turbulence. *Geophysical & Astrophysical Fluid Dynamics*, 111(3):209–227.

Resseguier, V., Mémin, E., Heitz, D., and Chapron, B. (2017d). Stochastic modelling and diffusion modes for POD models and small-scale flow analysis. *Journal of Fluid Mechanics*, 828:888–917.

Ruhnau, P., Kohlberger, T., Schnörr, C., and Nobach, H. (2005). Variational optical flow estimation for particle image velocimetry. *Experiments in Fluids*, 38(1):21–32.

Stapf, J. and Garbe, C. (2014). A learning-based approach for highly accurate measurements of turbulent fluid flows. *Experiments in Fluids*, 55(8):1799.

Su, L. K. and Dahm, W. J. (1996). Scalar imaging velocimetry measurements of the velocity gradient tensor field in turbulent flows. I. assessment of errors. *Physics of Fluids*, 8(7):1869–1882.

Sun, D., Roth, S., and Black, M. (2010). Secrets of optical flow estimation and their principles. In *Proceedings of the IEEE Conference on Computer Vision and Pattern Recognition (CVPR)*, pages 2432–2439. IEEE.

Tokumaru, P. T. and Dimotakis, P. E. (1995). Image correlation velocimetry. *Experiments in Fluids*, 19(1):1–15.

Yuan, J., Schnörr, C., and Mémin, E. (2007). Discrete orthogonal decomposition and variational fluid flow estimation. *Journal of Mathematical Imaging and Vision*, 28(1):67–80.